INTERNATIONAL JOURNAL FOR NUMERICAL METHODS IN FLUIDS
Int. J. Numer. Meth. Fluids 2004; **44**:377–407 (DOI: 10.1002/fld.646)

Employment of the second-moment turbulence closure on arbitrary unstructured grids

B. Basara*,†

AVL List GmbH, Advanced Simulation Technologies, Hans List Platz 1, Graz A-8020, Austria

SUMMARY

The paper presents a finite-volume calculation procedure using a second-moment turbulence closure. The proposed method is based on a collocated variable arrangement and especially adopted for unstructured grids consisting of 'polyhedral' calculation volumes. An inclusion of $\frac{2}{3}k$ in the pressure is analysed and the impact of such an approach on the employment of the constant static pressure boundary is addressed. It is shown that this approach allows a removal of a standard but cumbersome velocity–pressure –Reynolds stress coupling procedure known as an extension of Rhie-Chow method (AIAA J. 1983; **21**: 1525–1532) for the Reynolds stresses. A novel wall treatment for the Reynolds-stress equations and 'polyhedral' calculation volumes is presented. Important issues related to treatments of diffusion terms in momentum and Reynolds-stress equations are also discussed and a new approach is proposed. Special interpolation practices implemented in a deferred-correction fashion and related to all equations, are explained in detail. Computational results are compared with available experimental data for four very different applications: the flow in a two-dimensional 180° turned U-bend, the vortex shedding flow around a square cylinder, the flow around Ahmed Body and in-cylinder engine flow. Additionally, the performance of the methodology is assessed by applying it to different computational grids. For all test cases, predictions with the second-moment closure are compared to those of the k–ε model. The second-moment turbulence closure always achieves closer agreement with the measurements. A moderate increase in computing time is required for the calculations with the second-moment closure.

KEY WORDS: Reynolds averaged Navier–Stokes equations; Reynolds-stress model; finite volume method; arbitrary unstructured grids

1. INTRODUCTION

Confidence in CFD can be gained only by proving that basic errors of numerical simulations are efficiently reduced i.e. iteration, discretization and modelling errors. A discretization error which presents the difference between the exact solution of the differential equations and the exact solution of discretized algebraic system of equations can be reduced by grid refinement and by employing more accurate approximations. An iteration error, the difference between

*Correspondence to: B. Basara, AVL List GmbH, Advanced Simulation Technologies, Hans List Platz 1, A-8020 Graz, Austria.
†E-mail: branislav.basara@avl.com

Received 19 October 2002
Revised 14 April 2003

the iterative and the exact solution of the algebraic equation systems, can also be reduced to negligible levels. On the modelling side, turbulence models appear to be the largest and the most common source of error in Reynolds-averaged Navier–Stokes (RANS) based numerical simulations as the flows in practice are predominantly turbulent. Despite some progress in recent years, turbulence models still bring a lot of uncertainties into the use of CFD. So it is mandatory to use the most advanced and accurate turbulence models.

Nowadays, it is common practice to use unstructured grids. With the reduction of meshing time, even the 'poor quality' grids consisting of computationally awkward cells (e.g. higher aspect ratios, twisted faces, negative volumes, negative wall normal distances, small opening angles between two neighbouring faces etc.) are used in calculations. This undoubtedly leads to a high degradation of a convergence rate. In addition, it is more important to use higher order differencing schemes for all fluxes, because numerical solutions can be very dependent on the employed 'non-body fitted' grids. Uncertainties in definitions of boundary conditions may produce unexpected problems as well. Moreover, advanced and complex models like the second-moment closure require careful use and deeper understanding of the basic features of flows e.g. many oscillating convergence behaviours during steady state calculations may be related to capturing some transient phenomena and not to the model's numerical instability, and hence transient calculations are required to obtain numerically and physically accurate results. Therefore to date, the most common turbulence models implemented in CFD codes are of the eddy viscosity type e.g. standard k–ε, non-linear k–ε and k–ω models. Even though limitations of these models are very well known, they are used due to numerical robustness and the fact that parametric studies do not often require absolute accuracy but rather calculation of relative differences caused by specific parametric variations. However, more reliable and refined turbulence models than those of the eddy-viscosity type are clearly required. In the case of the second-moment closure, attempts of using it for complex industrial applications have been reported, but commercial CFD vendors still do not recommend it for 'everyday' applications. It seems that so far, a robust numerical algorithm is not available for the second-moment closure.

In the last decade, a number of papers have been reported on the implementation of the second-moment closure in finite volume codes e.g. References [1–4], etc. The starting point of most of the reported work in this area is the set of governing Reynolds-Averaged Navier–Stokes equations solved for dependent variables in Cartesian co-ordinates and by using collocated variable arrangements. The same approach is also used in many commercial CFD codes e.g. STAR-CD, FLUENT, CFX, AVL FIRE/SWIFT, etc. The advantages of this approach, like having a single set of computational cells covering a non-orthogonal calculation domain, easier implementation of boundary conditions and general simplicity without diminishing the accuracy of simulations, direct many CFD developers to follow such practice. Certainly, this method has weak points. The basic drawback is the coupling of velocity and pressure field due to the placement of velocity and pressure at the same calculation points. This problem is usually overcome by means of the well known Rhie and Chow [5] interpolation practice for the velocity prediction at the face of the control volume. However, higher grid distortions enhance the burden on this method very often bringing the whole procedure to the edge of usability.

Numerical algorithms based on the control volume method often differ in interpolation techniques employed which allow for different types of grids. The work in this paper is based on the latest and most advanced 'polyhedral' approach where the algorithm is adopted for

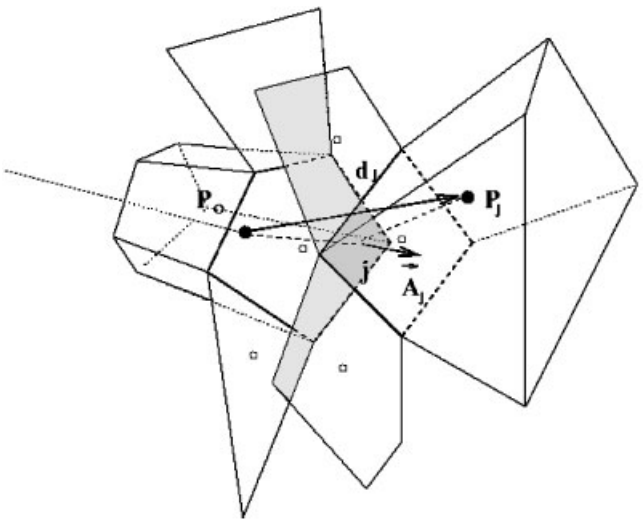

Figure 1. Calculation volumes and an arbitrary interface.

the calculations on control volumes consisting of arbitrary number of faces (see Figure 1). This allows an easy use of an arbitrary interface and a local grid refinement which further optimizes meshing as well as computing time [6–8]. But, such an approach further complicates the implementation of second-moment closures and even requires a special adoption of existing treatments. Therefore, the main objective of this paper is to describe a simple and efficient method for the employment of the second-moment closure for unstructured grids. The method proposed here can also be used for the employment of some simpler turbulence models e.g. non-linear k–ε or algebraic stress model. It is shown that some previous treatments are no longer necessary which simplifies a very complex implementation procedure. The paper concentrates on the main challenges: a treatment of diffusion term in momentum equations, implementation of the wall function in the Reynolds-stress equations, a treatment of diffusion in the Reynolds stress and dissipation rate equations, and an inclusion of $\frac{2}{3}k$ in the pressure to enhance coupling between pressure and turbulence field.

To demonstrate the numerical method, the Reynolds-stress model of Speziale *et al.* [9] is selected to represent the second-moment closure. Computational grids used for calculations include an arbitrary interface, a local grid refinement and all types of computational cells up to six faces (polyhedral volumes appear on the arbitrary interface). The results show that the second-moment closure can be used on unstructured grids and for real-life CFD applications.

2. MATHEMATICAL MODEL

The governing equations for the mass and momentum can be written in the Cartesian tensor notation as

$$\frac{\partial \rho}{\partial t} + \frac{\partial}{\partial x_j}(\rho U_j) = 0 \tag{1}$$

$$\frac{\partial}{\partial t}(\rho U_i) + \frac{\partial}{\partial x_j}(\rho U_i U_j) = -\frac{\partial p}{\partial x_i} + \frac{\partial}{\partial x_j}\left[\mu\left(\frac{\partial U_i}{\partial x_j} + \frac{\partial U_j}{\partial x_i} - \frac{2}{3}\frac{\partial U_k}{\partial x_k}\delta_{ij}\right) - \rho\overline{u_i u_j}\right] \tag{2}$$

where U_i stands for the mean velocity vector, p, ρ and μ are the pressure, the fluid density and the dynamic viscosity, respectively. Correlations $\overline{u_i u_j}$, known as Reynolds stresses, have to be defined before the momentum Equations (2) can be solved. For the calculation of the last test case presented in this paper, the flow in an intake port, the density is calculated from the equation of state, thus

$$\rho = \frac{p}{R_g T} \tag{3}$$

where R_g is the gas constant and T is the temperature.

With the k–ε eddy-viscosity model, the Reynolds stresses are evaluated from Bousinessq's assumption, given by

$$-\rho\overline{u_i u_j} = 2\mu_t S_{ij} - \frac{2}{3}\rho\delta_{ij}k \tag{4}$$

where S_{ij} is the mean rate of the stress tensor, given as

$$S_{ij} = \frac{1}{2}\left(\frac{\partial U_i}{\partial x_j} + \frac{\partial U_j}{\partial x_i}\right) \tag{5}$$

and turbulence viscosity μ_t is evaluated from

$$\mu_t = C_\mu \rho \frac{k^2}{\varepsilon} \tag{6}$$

In order to close the k–ε model, it is necessary to solve equations for the turbulence kinetic energy k and its dissipation rate ε:

$$\frac{\partial}{\partial t}(\rho k) + \frac{\partial}{\partial x_j}(\rho k U_j) = \rho(P_k - \varepsilon) + \frac{\partial}{\partial x_j}\left[\left(\mu + \frac{\mu_t}{\sigma_k}\right)\frac{\partial k}{\partial x_j}\right] \tag{7}$$

$$\frac{\partial}{\partial t}(\rho\varepsilon) + \frac{\partial}{\partial x_j}(\rho\varepsilon U_j) = \rho\left(C_{\varepsilon 1}P_k - \frac{2}{3}(2 - C_{\varepsilon 1})k\frac{\partial U_k}{\partial x_k} - C_{\varepsilon 2}\varepsilon\right)\frac{\varepsilon}{k} + \frac{\partial}{\partial x_j}\left[\left(\mu + \frac{\mu_t}{\sigma_\varepsilon}\right)\frac{\partial \varepsilon}{\partial x_j}\right] \tag{8}$$

where the production of turbulence energy is given by $P_k = -\overline{u_i u_j}\partial U_i/\partial x_j$. The model coefficients appearing in the above equations are assigned their standard values (standard k–ε model [10]):

$$C_\mu = 0.09, \quad C_{\varepsilon 1} = 1.44, \quad C_{\varepsilon 2} = 1.92, \quad \sigma_k = 1.0, \quad \sigma_\varepsilon = 1.3$$

The compressible correction term in the ε-equation is re-written in another form by using the continuity equation, thus

$$-\frac{2}{3}(2 - C_{\varepsilon 1})\rho\varepsilon\frac{\partial U_k}{\partial x_k} = \frac{2}{3}(2 - C_{\varepsilon 1})\varepsilon\left(\frac{\partial \rho}{\partial t} + U_k\frac{\partial \rho}{\partial x_k}\right) \tag{9}$$

For the last case in this paper, the flow in an intake port, the steady state calculations were sufficient as calculations were performed on static grids. Hence compressibility effects were included in the dissipation rate equation only via term $U_k(\partial\rho/\partial x_k)$, see Equation (9), which is relatively small for this type of flow so that the case can be considered as weakly compressible. The other test cases presented here are incompressible.

Nevertheless, it is well known that the standard k–ε model does not give adequate representation of the turbulence field in most cases and especially not in the flows where normal stresses and their anisotropy form a significant contribution to the momentum balance. Although the model has been improved for various purposes, the capability to predict certain flows and especially separated flows, is and will stay poor.

The second-moment closure adopted here is the high Reynolds number Reynolds-stress variant of Speziale, Sarkar and Gatski (SSG) [9]. Therefore, the Reynolds-stress equations given as

$$\frac{\partial}{\partial t}(\rho\overline{u_iu_j}) + \frac{\partial}{\partial x_j}(\rho\overline{u_iu_j}U_k) = P_{ij} + D_{ij} - \varepsilon_{ij} + \phi_{ij} \tag{10}$$

where a diffusion by turbulence fluctuations was modelled with the simple gradient-transport hypothesis (C_s equal to 0.22) and viscous dissipation was assumed to be isotropic, can then be written as

$$\begin{aligned}\frac{\partial}{\partial t}(\rho\overline{u_iu_j}) + \frac{\partial}{\partial x_k}(\rho\overline{u_iu_j}U_k) = &-\rho\left(\overline{u_iu_k}\,\frac{\partial U_j}{\partial x_k} + \overline{u_ju_k}\,\frac{\partial U_i}{\partial x_k}\right)\\ &+\frac{\partial}{\partial x_k}\left[\mu\,\frac{\partial\overline{u_iu_j}}{\partial x_k} + C_s\rho\,\frac{k}{\varepsilon}\,\overline{u_ku_l}\,\frac{\partial\overline{u_iu_j}}{\partial x_l}\right] - \frac{2}{3}\,\delta_{ij}\rho\varepsilon\\ &-\rho(C_1\varepsilon + C_1^*P_k)b_{ij} + \rho C_2\varepsilon\left(b_{ik}b_{jk} - \frac{1}{3}\,b_{mn}b_{mn}\delta_{ij}\right)\\ &+\rho[C_3 - C_3^*(b_{mn}b_{mn})^{1/2}]kS_{ij}\\ &+C_4\rho k\left(b_{ik}S_{jk} + b_{jk}S_{ik} - \frac{2}{3}\,b_{mn}S_{mn}\delta_{ij}\right)\\ &+C_5\rho k(b_{ik}W_{jk} + b_{jk}W_{ik})\end{aligned} \tag{11}$$

where $b_{ij} = \overline{u_iu_j}/(2k) - \delta_{ij}/3$ and $W_{ij} = 0.5(\partial U_i/\partial x_j - \partial U_j/\partial x_i)$ are the Reynolds-stress anisotropy and the mean vorticity tensors respectively. The dissipation rate was obtained from the standard equation:

$$\begin{aligned}\frac{\partial}{\partial t}(\rho\varepsilon) + \frac{\partial}{\partial x_j}(\rho\varepsilon U_j) = &\rho\left(C_{\varepsilon1}P_k - \frac{2}{3}(2 - C_{\varepsilon1})k\,\frac{\partial U_k}{\partial x_k} - C_{\varepsilon2}\varepsilon\right)\frac{\varepsilon}{k}\\ &+\frac{\partial}{\partial x_j}\left(\mu\,\frac{\partial\varepsilon}{\partial x_j}\right) + \frac{\partial}{\partial x_j}\left(C_\varepsilon\rho\,\frac{k}{\varepsilon}\,\overline{u_iu_j}\,\frac{\partial\varepsilon}{\partial x_j}\right)\end{aligned} \tag{12}$$

A turbulence kinetic energy k is obtained from the sum of the normal Reynolds stresses $k = \frac{1}{2} \sum \overline{u_i u_i}$. The model constants of the Reynolds stress transport model based on the SSG pressure-strain formulation are as follows, Speziale *et al.* [9]:

$$C_1 = 3.4, \quad C_1^* = 1.8, \quad C_2 = 4.2, \quad C_3 = 0.8, \quad C_3^* = 1.3, \quad C_4 = 1.25$$

$$C_5 = 0.4, \quad C_s = 0.22, \quad C_\varepsilon = 0.183, \quad C_{\varepsilon 1} = 1.44, \quad C_{\varepsilon 2} = 1.83$$

It is widely accepted that second-moment turbulence closures offer in principle a better physical basis for modelling complex non-equilibrium turbulent flows. Separation and recirculation regions, strong streamline curvatures, impingement and strong three-dimensionality are only some of the features better reproduced by second-moment closures when compared with the k–ε model.

3. NUMERICAL PROCEDURE

The discretization of the governing differential equations is obtained using a cell-centred finite volume approach. In the method used here, the governing equations are integrated, term-by-term, over the 'polyhedral' control volumes, see Figure 1. Such discretization practice was recently explored in other publications starting with Demirdzic and Muzaferija [6], and continuing with Ferziger and Peric [7], Marthur and Marthy [8] etc. Hence the method has been applied and proved on various applications. The method rests on the integral form of the general conservation law. Thus, for the control volume with the outward surface (cell-face) vectors $\mathbf{A} = A_k \mathbf{i}_k$, all modelling equations can be described as

$$\underbrace{\frac{\mathrm{d}}{\mathrm{d}t} \int_V \rho\phi \, \mathrm{d}V}_{\text{Rate of change: } R} + \underbrace{\oint_A \rho\phi U_k \, \mathrm{d}A_k}_{\text{Convection: } C} = \underbrace{\oint_A \Gamma_\phi^{kk} \frac{\partial \phi}{\partial x_k} \, \mathrm{d}A_k}_{\text{Diffusion: } D} + \underbrace{\int_V s_\phi^V \, \mathrm{d}V + \oint_A s_{\phi k}^A \, \mathrm{d}A_k}_{\text{Sources: } S} \tag{13}$$

where a general variable $\phi(x_k, t)$ can represent either scalars or vector and tensor field components. Here, the Cartesian coordinate system (x, y, z) with the unit vectors $(\mathbf{i}, \mathbf{j}, \mathbf{k})$ is used and tensor notation is employed. In the above equation, ρ is the fluid density, t is time, U_k are components of the fluid velocity vector, Γ_ϕ^{kk} is the diffusion coefficient for the variable ϕ (in this case repeated indices do not imply summation), s_ϕ^V and $s_{\phi k}^A$ are the volumetric and surface source terms, respectively. The cell-face based connectivity and interpolation practices for gradients and cell-face values are introduced to accommodate an arbitrary number of cell faces. A second-order midpoint rule is used for integral approximation. In terms of the notation shown in Figure 1 for a typical grid cell P with the volume V surrounded by it's neighbours P_j, the discretized control volume equation can be written as

$$\frac{\mathrm{d}}{\mathrm{d}t}(\rho_P V_P \phi_P) + \sum_{j=1}^{n_f} C_j - \sum_{j=1}^{n_f} D_j = (s_\phi^V)_P V_P + \sum_{j=1}^{n_f} (s_{\phi k}^A A_k)_j \tag{14}$$

where C_j and D_j are convective and diffusion transport through the face j, respectively, and n_f is the number of cell-faces.

With the use of linear interpolation, the cell face values can be calculated as

$$\phi_j = f_j \phi_p + (1 - f_j)\phi_{p_j} \tag{15}$$

where f_j is the cell face interpolation factor. In the case that the vector connecting two centres P and P_j does not pass through the face centre, one can introduce a correction term as suggested by Demirdzic and Muzaferija [6], thus

$$\phi_j = \phi_{j'} + \nabla\phi_{j'}(\mathbf{r}_j - \mathbf{r}_{j'}) \tag{16}$$

where the point j' can be the midpoint between centres P and P_j. Following this, f_j is equal to 0.5 and the vector between points j and j' can be easily computed.

The cell gradients can be calculated by using either the Gauss' theorem, thus

$$\nabla\phi_p = \frac{1}{V_p} \sum_{j=1}^{n_f} \phi_j \mathbf{A}_j \tag{17}$$

or a linear least-square approach e.g. Muzaferija [11]. Using Gauss' theorem and with the simple mathematical reconstructions to replace vertex values only with the contributions from cells P and P_j, one can arrive at the following formula for the cell face gradient, thus

$$\nabla\phi_j = \overline{\nabla\phi}_j + \frac{\mathbf{A}_j}{\mathbf{A}_j\mathbf{d}_j}\left[(\phi_{P_j} - \phi_P) - \overline{\nabla\phi}_j \cdot \mathbf{d}_j\right] \tag{18}$$

where

$$\overline{\nabla\phi_j} = f_j \nabla\phi_p + (1 - f_j)\nabla\phi_{p_j} \tag{19}$$

These interpolation practices are used to derive the terms in the discretized Equation (14) as presented below.

3.1. Diffusion term

One of the key points for the efficient implementation of the second-moment closure is the treatment of diffusion terms. To simplify this task and to make a numerical code more modular, some equations are rewritten in order to always get an isotropic diffusion coefficient while the rest of the terms are introduced as volumetric source terms on the right-hand side of the equations. Treating these sources in a deferred correction manner by using values from the previous iteration step, a complete numerical algorithm is further stabilised. For example, a diffusion term given in Equation (11) for the Reynolds-stresses is reformulated before discretization, thus

$$\frac{\partial}{\partial x_k}\left[\mu \frac{\partial \overline{u_i u_j}}{\partial x_k} + C_s\rho \frac{k}{\varepsilon}\overline{u_k u_l}\frac{\partial \overline{u_i u_j}}{\partial x_l}\right] = \frac{\partial}{\partial x_k}\left[\mu_{\text{eff}} \frac{\partial \overline{u_i u_j}}{\partial x_k} + C_s\rho \frac{k}{\varepsilon}\overline{u_k u_l}\frac{\partial \overline{u_i u_j}}{\partial x_l} - \mu_t \frac{\partial \overline{u_i u_j}}{\partial x_k}\right] \tag{20}$$

as well as a diffusion term from the dissipation rate equation is now written as

$$\frac{\partial}{\partial x_j}\left[\mu \frac{\partial \varepsilon}{\partial x_j} + C_s\rho \frac{k}{\varepsilon}\overline{u_i u_j}\frac{\partial \varepsilon}{\partial x_j}\right] = \frac{\partial}{\partial x_j}\left[\mu_{\text{eff}} \frac{\partial \varepsilon}{\partial x_j} + C_s\rho \frac{k}{\varepsilon}\overline{u_i u_j}\frac{\partial \varepsilon}{\partial x_j} - \mu_t \frac{\partial \varepsilon}{\partial x_j}\right] \tag{21}$$

where $\mu_{\text{eff}} = \mu + \mu_t$ is effective dynamic viscosity.

Therefore, a common isotropic diffusion coefficient can be extracted for all equations, e.g. for Equations (20) and (21) an isotropic diffusion part is given as

$$\frac{\partial}{\partial x_k}\left[\mu_{\text{eff}}\frac{\partial \overline{u_i u_j}}{\partial x_k}\right] \quad \text{and} \quad \frac{\partial}{\partial x_k}\left[\mu_{\text{eff}}\frac{\partial \varepsilon}{\partial x_k}\right] \tag{22}$$

Using Equation (18) for cell face gradients, the diffusion term can be written as

$$D_j = \underbrace{\bar{\Gamma}_{\phi j}\frac{\mathbf{A}_j^2}{\mathbf{A}_j\mathbf{d}_j}(\phi_{P_j}-\phi_P)}_{\text{normal-diffusion}} + \underbrace{\bar{\Gamma}_{\phi j}\overline{\nabla\phi}_j\left(\mathbf{A}_j-\frac{\mathbf{A}_j^2}{\mathbf{A}_j\mathbf{d}_j}\mathbf{d}_j\right)}_{\text{cross-diffusion}} \tag{23}$$

and used in the same form for all equations. The cross-diffusion part of Equation (23), which vanishes on the orthogonal grid, is introduced in discretized equations as surface source term, see Equation (14). Obviously, a diffusion coefficient μ_{eff} is used for turbulence kinetic energy and dissipation rate equations defined with the standard k–ε model but also now for Reynolds stresses defined with the Reynolds-stress model. The remainder of Equations (20) and (21) goes in the discretized equation (14) as a volumetric source after applying Gauss' theorem or a least-square method. With this approach, diffusion terms in all equations can be solved with the same part of code just replacing diffusion coefficients and source terms.

For the momentum equations, a diffusion term is derived from $\mu(\partial U_i/\partial x_j) - \rho\overline{u_i u_j}$, where $\overline{u_i u_j}$ are Reynolds stresses obtained from their own transport equation in the case of the Reynolds stress model or from different assumptions depending on the model employed e.g. Boussinesq's formula for k–ε model. It is clear that in the case of the standard k–ε model, a diffusion term has the same form as given with Equation (22), see Equations (2) and (4). For the second-moment closure, further manipulations are required to get a more suited form for discretization. The Reynolds stresses predicted by the second-moment closure are introduced in the momentum equations using the following formulation [12, 13]:

$$\overline{u_i u_j} = \underbrace{\overline{u_i u_j}_{\text{iso}}^{k-\varepsilon}}_{A\text{:source+diffusion}} + \underbrace{\overline{u_i u_j}_{\text{model}} - \overline{u_i u_j}_{\text{iso}}}_{B\text{:source}} \tag{24}$$

where $\overline{u_i u_j}_{\text{iso}}$ is an 'isotropic' part defined by Boussinesq's formula and $\overline{u_i u_j}_{\text{model}}$ are obtained from the Reynolds-stress equations. Equation (24) can be now written as

$$\overline{u_i u_j} = -2\nu_t S_{ij} + \frac{2}{3}k\delta_{ij} + \overline{u_i u_j}_{\text{model}} - \overline{u_i u_j}_{\text{iso}} \tag{25}$$

If we take $\overline{u_i u_j}_{\text{iso}} = -2\nu_t S_{ij} + \frac{2}{3}k\delta_{ij}$ then the term $\frac{2}{3}k\delta_{ij}$ can be incorporated in the pressure following common practice applied for the k–ε model [14] (see Equations (2) and (4)). This means that the pressure is now collectively represented by $p + \frac{2}{3}k$. Therefore, in addition to the normal and cross diffusion from the term $2\nu_t S_{ij}$ as in the standard k–ε model (see Equation (24)), the underlined term on the right-hand side of the momentum equations (see Equation (2)) appears as

$$-\frac{\partial p}{\partial x_i} + \frac{\partial}{\partial x_j}\left[\mu_{\text{eff}}\left(\frac{\partial U_i}{\partial x_j}+\frac{\partial U_j}{\partial x_i}\right)\right] - \underline{\frac{\partial}{\partial x_j}\left(\overline{\rho u_i u_j}_{\text{model}} - \frac{2}{3}\rho k\delta_{ij} + 2\mu_t S_{ij}\right)}$$

which is then introduced in the discretized Equation (14) as a volumetric source term after applying Gauss' theorem or a least-square method. Note that the same procedure can also be used for some other models, e.g. $\overline{u_i u_j}_{\text{model}}$ can be derived by the algebraic stress model. This procedure is also useful for zonal modelling as the models can be changed from cell to cell in one line of code.

3.2. Pressure–velocity coupling

The overall solution procedure is iterative and is based on the SIMPLE [15] algorithm. In this algorithm, a pressure-correction equation is derived from the discretized equations for continuity and momentum. The discretized momentum equation for node P can be written as

$$\mathbf{U}_P = \frac{\sum_{j=1}^{n_f} a_j \mathbf{U}_{P_j} + S_u}{a_P} - \frac{V_P}{a_P} \nabla p_P \tag{26}$$

where the pressure gradient is treated separately from the sources S_u. The cell-face velocities are now obtained by interpolation of the above equation and inclusion of the pressure gradient directly on the face [1, 6, 14], thus

$$\mathbf{U}_j^* = \bar{\mathbf{U}}_j - \overline{\left(\frac{V}{a_P}\right)}_j (\nabla p_j - \overline{\nabla p}_j) \tag{27}$$

After replacing the pressure gradient ∇p_j by the face gradient, the face velocity can be calculated as

$$\mathbf{U}_j^* = \bar{\mathbf{U}}_j - \frac{1}{2}\left(\frac{V_P}{a_P} + \frac{V_{P_j}}{a_{P_j}}\right) \frac{\mathbf{A}_j}{\mathbf{A}_j \cdot \mathbf{d}_j} \left[(p_{P_j} - p_P) - \overline{\nabla p}_j \cdot \mathbf{d}_j\right] \tag{28}$$

where the overbars signify terms calculated by linear interpolation from nodes P and P_j.

By starting from a guessed pressure field, the calculated velocities do not necessarily satisfy the continuity equation and so a correction has to be introduced to those velocities in order to ensure this. The role of this correction can be seen from considering the discretized form of the continuity equation, expressed as

$$\frac{\mathrm{d}}{\mathrm{d}t}(\rho_P^* V_P) + \sum_{j=1}^{n_f} \dot{m}_j^* = S_m \tag{29}$$

The quantity S_m represents a false mass source which should disappear when a converged solution is attained. The simple form of the face velocity correction needed to enforce a continuity can be written as

$$\mathbf{U}_j' = -\overline{\left(\frac{V}{a_P}\right)}_j \frac{\mathbf{A}_j}{\mathbf{A}_j \cdot \mathbf{d}_j} (p'_{P_j} - p'_P) \tag{30}$$

By substituting the velocities by their corrections, mass flux corrections $\dot{m}_j'$ are obtained and those are then used to obtain the corrected fluxes, thus:

$$\dot{m}_j = \dot{m}_j^* + \dot{m}_j' \tag{31}$$

Manipulation of the above now gives

$$\sum_{j=1}^{n_f} \dot{m}'_j + S_m = 0 \tag{32}$$

This combined with Equation (30) yields the pressure correction equation:

$$a'_P p'_P = \sum_{j=1}^{n_f} a'_{P_j} p'_{P_j} - S_m \tag{33}$$

The solution of this equation yields the pressure corrections p', which are now used to evaluate the velocity corrections from Equation (30) and obtain new field values. Again, the newly corrected values are used in the solution of the momentum and pressure-correction equations until convergence is attained.

For the second-moment closure, Obi [16] introduced Reynolds-stresses next to the pressure in Equation (28) to couple velocities and pressure additionally with the Reynolds-stresses (see also Reference [17]). This method is denoted here as method-1. Nevertheless, in the case of non-orthogonal control volumes, the Reynolds-stresses at the face of the control volume have to be calculated in the local coordinate system in which one axis is normal to the face. This might be very cumbersome procedure, see original reference [16]. Basara and Younis [18] did a similar coupling approach but only taking into account the positive part of the projected Reynolds-stresses to ensure stronger coupling between these variables. However, this approach is abandoned here as one part of the turbulence field is directly included in the solution of the pressure correction equation, namely $(p + \frac{2}{3}k)$ and then directly coupled with the mean flow via Equation (28), the same approach applied as for the standard k–ε model. When comparing convergence rate in certain cases, it is not obvious which method is more efficient but the simplicity of the method-2 for non-orthogonal grids, less programming lines and better suitability for the pressure boundary (see Section 3.3.2), should give an advantage to the new proposed method. Here, as a simple example, the convergence rate for the calculation of developing flow in a straight duct are shown in Figure 2. The mass residuals obtained by using method-2 shows that better convergence is obtained than in the case when method-1 is used. This is due to the employment of the pressure boundary specified at the outlet of the duct, see Section 3.3.2. Otherwise, both methods should perform similarly.

An analogous approach was used in the past by many authors (e.g. References [2, 4]) to calculate the Reynolds-stresses on the faces directly coupled with velocity field, but here this practice was found to be unnecessary when the special interpolation practice was used in conjunction with the deferred correction approach for diffusion terms as explained in Section 3.1.

Figure 3(a) shows the streamlines for the backward facing step as predicted by RSM using the procedure described above. It is evident that an unrealistic rearward streamline curvature at the end of separation is predicted as reported elsewhere e.g. References [2, 18–20]. However, looking at that region (the part of the solution very sensitive to a coupling approach and a wall treatment also), see Figure 3(b), it is clear that the predicted velocity has a very smooth distribution and no signs of de-coupled ‘zig-zag’ solution.

3.3. Boundary conditions

The convection and diffusion fluxes on the boundaries are calculated the same as for the internal faces. For the diffusion flux, Equation (23) is used and the upwind scheme for the

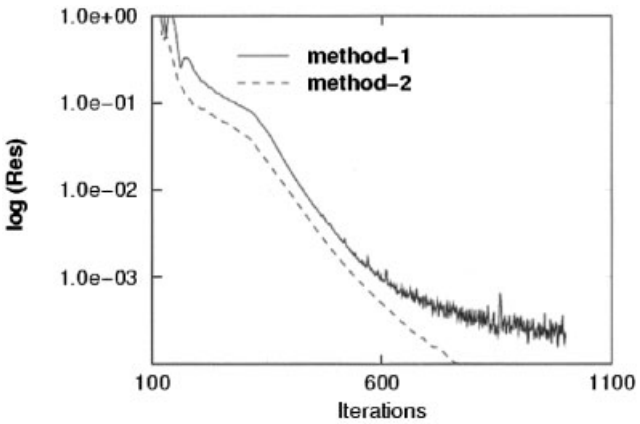

Figure 2. Convergence rate history by computation of a straight duct using the 'standard' method-1, extended Rhie and Chow method [5] with inclusion of the Reynolds stresses and the new method-2 incorporating $\frac{2}{3}k$ in pressure.

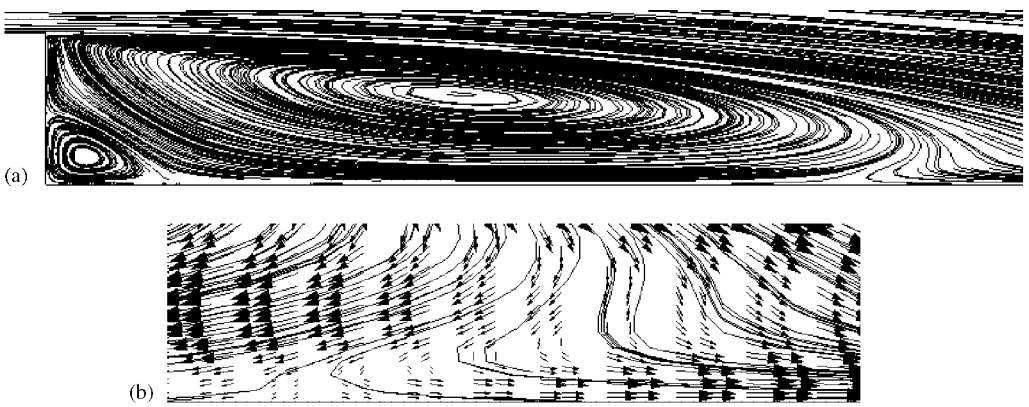

Figure 3. Streamlines (a) and velocity vectors in the area of an unrealistic rearward streamline curvature at the end of separation (b) as predicted by the Reynolds-stress model.

convection flux. The types of boundaries explained here in more detail are the wall boundary and the pressure boundary due to specific issues regarding the implementation of the second-moment closure.

3.3.1. Wall boundary. In this study, both of the models have been used only in conjunction with standard wall functions. In the momentum equations, the wall functions are implemented

by defining the effective near-wall turbulent viscosity as

$$\mu_w = \mu \frac{y_P^+}{U_P^+}, \quad U_P^+ = \begin{cases} y_P^+ & \text{if } y_P^+ < 11.63 \\ \dfrac{1}{\kappa} \ln(E y_P^+) & \text{if } y_P^+ \geqslant 11.63 \end{cases} \tag{34}$$

with $\kappa = 0.41$ and $E = 9$. The non-dimensional wall distance y_P^+ is given as

$$y_P^+ = \frac{\rho_P C_\mu^{\frac{1}{4}} k_P^{\frac{1}{2}} \delta n}{\mu} \tag{35}$$

where δn denotes the normal distance from the near-wall node P (the node closest to the wall) to the wall.

For the turbulent kinetic energy equation, the flux of turbulence kinetic energy at the wall is taken to be zero, a condition simply enforced by setting the appropriate finite-difference coefficients to zero. The values of k at the node closest to the wall is therefore obtained from the solution of its equation. A single modification to the standard equation is required: it concerns the way in which the rate of production of k is evaluated at the grid closest to the wall. Dissipation rate ε is fixed for the first-to-wall cells by assuming that turbulence is in local equilibrium, $\varepsilon_P = C_\mu^{3/4} k_P^{3/2}/(\kappa \Delta n_P)$. In the case of Reynolds stresses there are two main approaches, the first one was proposed by Lien and Leschziner [3] who derived the Reynolds-stresses in the first-to-wall cell by focusing on the stress equations, see Equation (11), applicable to local energy equilibrium. The 'log-law' derived stresses are wall-oriented and should be transformed to the Cartesian co-ordinate system to be in agreement with the procedure required for non-orthogonal geometry. The second approach in which the Reynolds-stress components are solved at the nodes closest to the wall seems to be more robust but is complicated to implement with wall functions. A simple treatment has been proposed by Basara [12, 21] to ensure 'reasonable' values of velocity gradients by using the log law. Thus:

$$\frac{\partial U_P}{\partial n} = \frac{\sqrt{\tau_{\text{wall}}/\rho}}{\kappa \delta n} \tag{36}$$

where τ_{wall} is the wall shear stress defined with the standard wall function approach by using velocity at the near wall cell parallel to the wall U_P. 'Very near' wall velocity aligned with the wall can be derived from Equation (36), thus:

$$|\mathbf{U}_{\text{wall}}| = |\mathbf{U}_P| - \frac{1}{\kappa} \sqrt{\tau_{\text{wall}}/\rho} \tag{37}$$

Additional 'smoothing of sources' for unstructured grids and polyhedral control volumes can be made by calculating $\nabla \mathbf{U}$ in the first to wall cells by using available $\mathbf{U}_{\text{wall}}$ from Equation (37). Then a new velocity can be re-calculated as

$$\mathbf{U}_{\text{Iface}} = \mathbf{U}_P + \delta \mathbf{l} \cdot \nabla \mathbf{U} \tag{38}$$

where $\mathbf{U}_{\text{Iface}}$ is at an imaginary face (IF) placed at the distance δ_n from the cell centre P (P is the centre between the wall and IF), see Figure 4. $\delta \mathbf{l}$ is the vector between P and IF. Now,

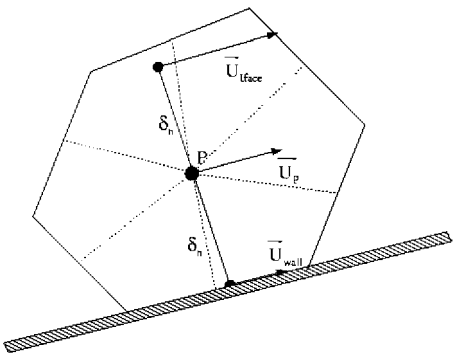

Figure 4. Near-wall boundary cell.

the 'very near' wall velocity can be recalculated as

$$|\mathbf{U}_{\text{wall}}^{\text{corr}}| = |\mathbf{U}_{\text{Iface}}| - \frac{2}{\kappa}\sqrt{\tau_{\text{wall}}/\rho} \tag{39}$$

As for the standard wall function, it is assumed that turbulent stress across the near wall cell is constant and is taken as being equal to the wall shear stress. Finally using the 'near-wall' velocity from Equation (39), production stress terms can be updated with the velocity gradients which now correspond to the 'log-law' velocity gradient in the direction normal to the wall. Such predicted Reynolds-stresses when introduced to momentum equations fit much better to the wall stresses predicted from the wall functions. Otherwise very fine grid distribution near the wall is required to get smooth velocity profiles on the wall. However, a difference between Equations (37) and (39) and with that, a difference between calculated velocity gradients near the wall, is decreased and the results are further improved by the following simple correction of the stress production. The production of turbulence kinetic energy can be obtained by summing up the production stress terms $P_k^{\text{eq}} = \frac{1}{2}P_{ii}$ and then compared with the production term obtained from the log law $P_k^{wf} = \tau_{\text{wall}}(\partial \mathbf{U}_P/\partial n)$ in order to provide a correction factor $f = P_k^{wf}/P_k^{\text{eq}}$ which is then used to correct stress production terms in Reynolds-stress equations.

Direct Numerical Simulation data of Kim *et al.* [22] for the fully developed turbulent flow with $Re = 13750$ in a plane channel was used for comparisons. The log law considering velocity distribution is well captured as shown in Figure 5. The distribution of normal stress components and their anisotropy is also fairly well described, see Figure 6. It should be pointed out that y^+ value at the first near to wall cell was 12.5. For the curved channel measured by Hunt and Joubert [23], shown in Figure 7(a), two different grids, a structured grid (see Figure 7(b)) and an unstructured grid consisting of tetrahedral internally and prismatic elements on the wall (see Figure 7(c)), were employed to check the implementation of the wall functions. The predicted velocity profiles at the outlet of the channel are in a good agreement with the measurements as shown in Figure 8.

3.3.2. Pressure boundary. The pressure boundary is frequently used in many real-life CFD applications. Usually the constant value for the pressure is prescribed across the boundary.

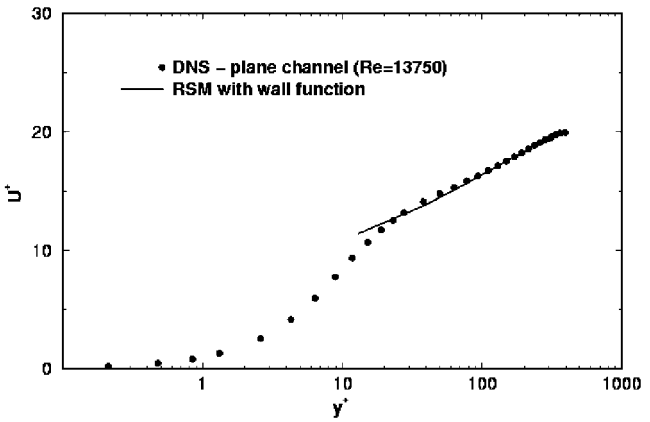

Figure 5. Computed mean velocity in a plane channel. Symbols: DNS, Kim *et al.* [22].

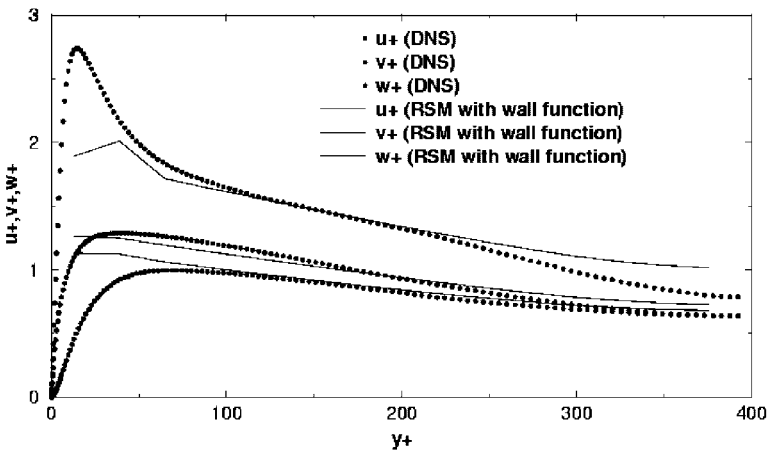

Figure 6. Computed stress components in a plane channel. Symbols: DNS, Kim *et al.* [22].

Following Equation (28), the boundary velocity can be obtained from:

$$\mathbf{U}_\mathrm{b} = \mathbf{U}_P - \left(\frac{V_P}{a_P}\right) \frac{\mathbf{A}_\mathrm{b}}{\mathbf{A}_\mathrm{b} \cdot \mathbf{d}_\mathrm{b}} [(p_\mathrm{b} - p_P) - \nabla p_P \cdot \mathbf{d}_\mathrm{b}] \tag{40}$$

and the velocity correction at the pressure boundary can then be approximated as

$$\mathbf{U}'_\mathrm{b} \approx -\left(\frac{V_P}{a_P}\right) \frac{\mathbf{A}_\mathrm{b}}{\mathbf{A}_\mathrm{b} \cdot \mathbf{d}_\mathrm{b}} (p'_b - p'_P) \tag{41}$$

where the pressure boundary correction is set to zero, $p'_b = 0$. Figure 9 shows the iso-lines of $(p + \frac{2}{3}k)$ predicted by k–ε model and (p) predicted by RSM model (this time with no

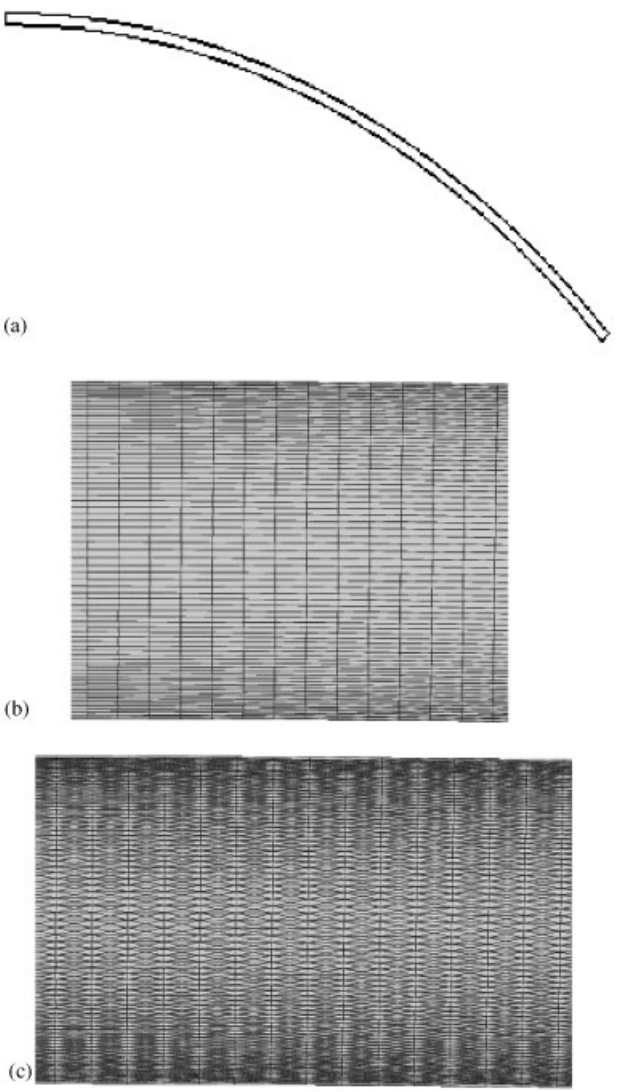

Figure 7. Computational domain (a), hexahedral grid (b) and tetrahedral grid (c) used for calculations.

incorporated $\frac{2}{3}k$). Now, it is clear that the definition of the constant value at the boundary, in this case at the outlet, matches the predictions with the k–ε model. Hence the term $\frac{2}{3}k$ is incorporated in the pressure for the second-moment closure as shown in Section 3.1. New predictions as shown in Figure 10, will be more consistent with the constant pressure or with the constant $(p + \frac{2}{3}k)$ actually at the boundary and with that, a better convergence rate can be expected (see Figure 2). Note that for the developed flow in a plane channel, it can be

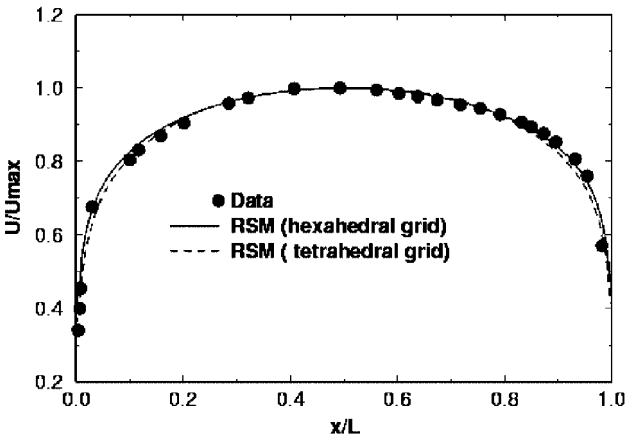

Figure 8. Computed mean velocity at the exit of the curved channel. Symbols: Measurements Hunt *et al.* [23].

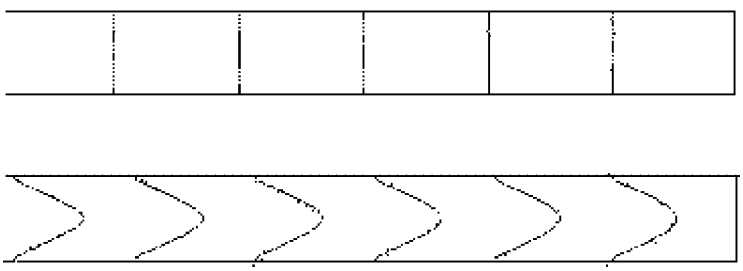

Figure 9. Iso-lines of $(p+\frac{2}{3}k)$ predicted by the k–ε model (top) and (p) predicted by RSM (bottom).

written for the y-normal to the flow direction that

$$0 = -\frac{\partial p}{\partial y} + \frac{\partial}{\partial y}(-\rho\overline{v^2}) \tag{42}$$

Therefore, when the normal stress $\overline{v^2}$ is incorporated in the pressure or $(p+\overline{v^2})$, the predicted 'iso-lines' will be the nearest to the constant value (have in mind that this was not a fully developed channel flow but close to that) as shown in Figure 10. However, it is more practical to include the term $\frac{2}{3}k$ in the pressure as done in this work than to search for appropriate Reynolds-stress components.

3.4. Other computational details

A deferred correction approach is also used for the treatment of convection fluxes, thus

$$C_j = \dot{m}_j \phi_j^{UDS} + \underline{\gamma_\phi |\dot{m}_j| \varphi_j (\phi_{P_j} - \phi_P)} \tag{43}$$

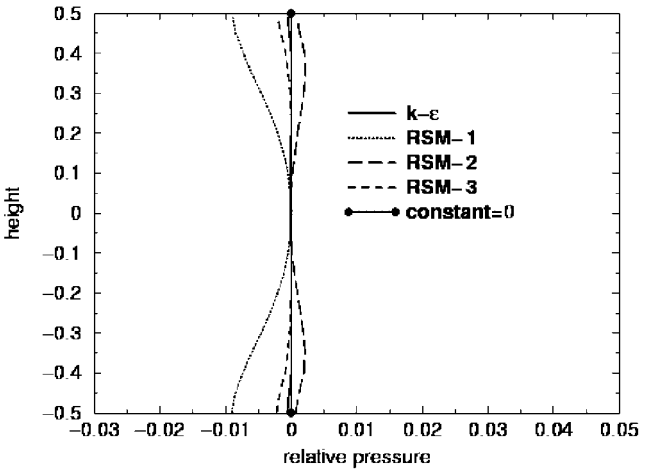

Figure 10. Iso-lines of $(p+\frac{2}{3}k)$ predicted by the k–ε model, (p), $(p+\frac{2}{3}k)$ and $(p+\overline{v^2})$ predicted by RSM (RSM-1, RSM-2 and RSM-3, respectively) in a plane channel.

where mass flux $\dot{m}_j$ is given as $\dot{m}_j = \rho \mathbf{U}_j \mathbf{A}_j$, and γ_ϕ is the blending factor between UDS and higher order scheme ($0 \leqslant \gamma \leqslant 1$). The underlined term is calculated by using values from the previous iteration step. The flux limiter φ_j is provided by the higher order differencing scheme used to ensure a bounded solution. In this work, the SMART (AVL SMART as proposed by Przulj and Basara [24]) and MINMOD [25] schemes were used as a compromise between accuracy and convergence properties.

The rate of change (see Equation (13)) is discretized by two implicit schemes, namely first order accurate Euler (two level) scheme and second order accurate three time level scheme.

The outcome of all presented above is a set of algebraic equations: one for each control volume and for each transport equation. An algebraic equation can be written concisely as

$$a_P \phi_P = \sum_{j=1}^{n_f} a_j \phi_{P_j} + S_\phi \tag{44}$$

where n_f is the number of internal cell-faces; a_P and a_j are coefficients and S_ϕ is the source term. Thus, for a computational domain with M control volumes, a system of $M \times N$ algebraic equations needs to be solved for N dependent variables ϕ. Each equation for the given variable is decoupled by treating other variables as known, which leads to a sub-set of M linear algebraic equations for each dependent variable. The linearized algebraic equations are solved by preconditioned conjugate gradient methods. The symmetric gradient method is used to solve equations with the symmetric matrix and the biconjugate method (Bi-CGSTAB) of Van Der Vorst [26] for equations with asymmetric matrix. Both methods are used with an incomplete Cholesky preconditioning technique [27].

4. RESULTS AND DISCUSSIONS

The performance of the methodology described above is assessed here in the following examples: a 180° turn-around duct, a vortex shedding flow around a square cylinder, a 3D Ahmed

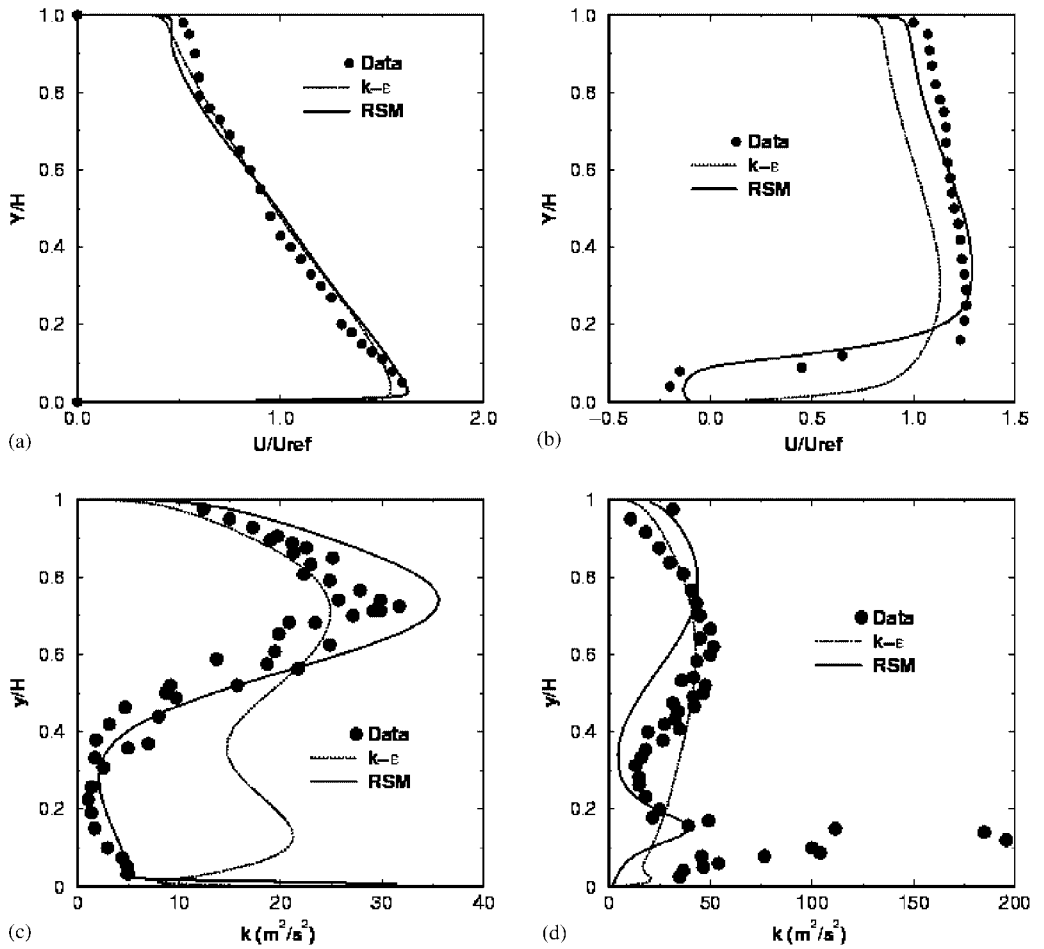

Figure 11. Mean velocity and kinetic energy profiles at two selected locations along the flow in a 180° turned U-bend: (a) and (c) at 90° and (b) and (d) at 180°.

idealized car model and a 3D intake port. The aim is to show applicability of the proposed numerical algorithm and not to analyse the results in detail.

The first example is based on the data of Monson *et al.* [28] in a 180° turn-around duct formed from a rectangular channel with an aspect ratio of 10. The flow is two dimensional along the mid-plane and the results obtained in this work are reported for the Reynolds number of 10^6. The results predicted with the k–ε model and the full Reynolds-stress model are almost identical to the predictions of Basara *et al.* [29] who reported a grid independent solution and are very similar to other model's performances reported elsewhere e.g. Shur *et al.* [30]. Therefore, it is also assumed that the grid of 22 000 computational cells used in this work, is sufficiently fine not to influence turbulence models testing. The challenge for the turbulence models is to predict the separation region after the bend. Figures 11(a) and (b) compared the predicted and measured axial mean-velocity profiles at two locations

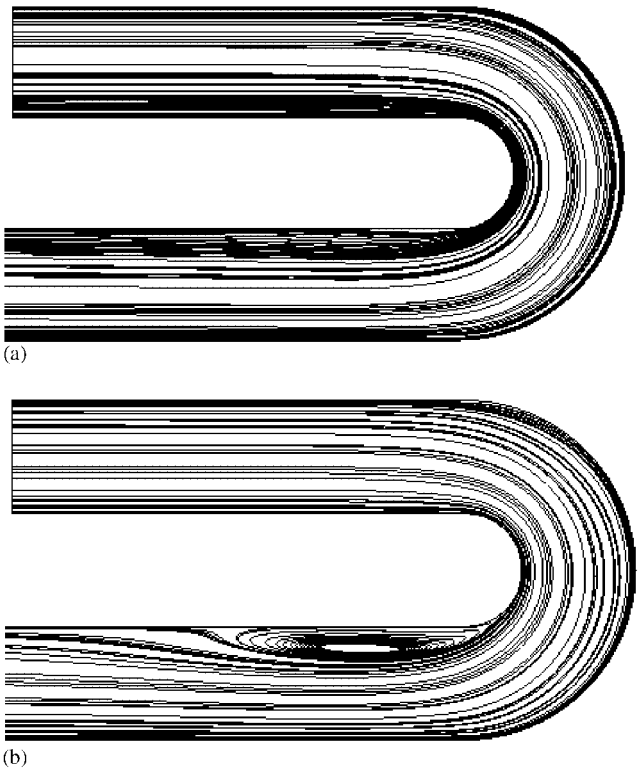

Figure 12. Streamline patterns of the flow in 180° turned U-bend obtained by the standard k–ε model (a) and the Reynolds-stress model (b).

within the bend at 90° and 180°. The RSM model captures the velocity profile shape at both positions quite contrary to the k–ε model. It is also clear that the turbulence kinetic energy is well predicted with the Reynolds-stress model, see Figures 11(c) and (d). The differences between the models are quite substantial, especially in the region closest to the inner wall. The trend predicted with the k–ε model is completely wrong. A reduction of the turbulence kinetic energy near the convex wall predicted with the RSM model causes the boundary layer to be less able to withstand the adverse pressure gradients encountered on entry to the duct with the result that flow detaches from the surface. The predicted streamlines are shown in Figure 12. The measured skin-friction coefficients (see Monson *et al.* [28]) suggest that the predicted size of the separation bubble by the Reynolds-stress model is approximately correct. The use of the correction for the production of turbulence kinetic energy as given in Section 3.3.1, causes a smoother attachment at the end of the separation bubble than shown in previous reported predictions, e.g. Basara *et al.* [29]. The Reynolds-stress model was switched on after performing a few hundred iterations with the k–ε model, but there is no need to wait for the full converged solution with the k–ε model before continuing with the RSM model. The difference in the computing time was around twice and the

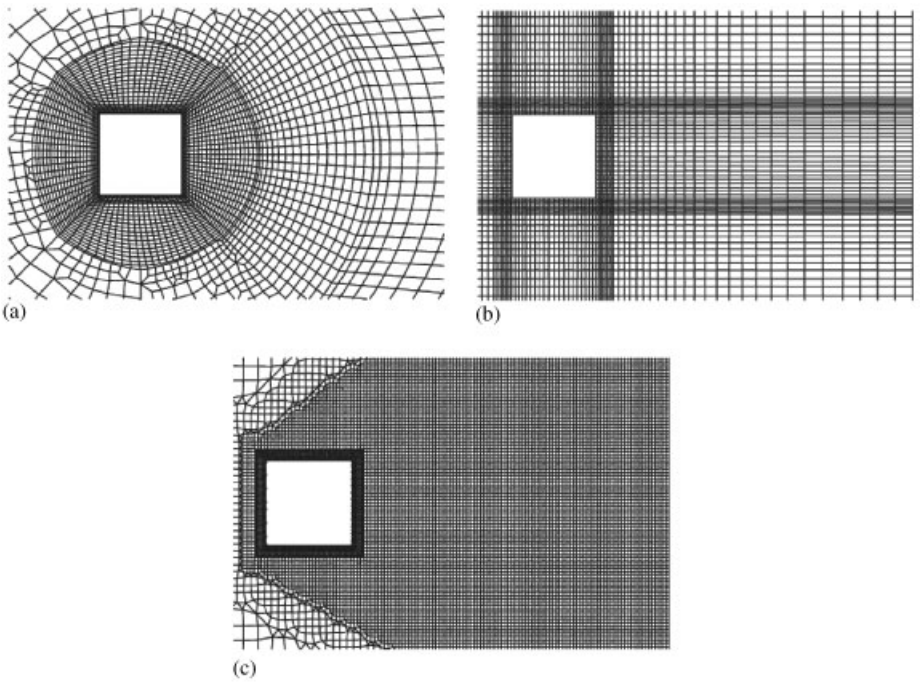

Figure 13. Details of the grids used for calculations: (a) 6822, (b) 21 800 and (c) 65 397 computational cells.

memory required for the Reynolds-stress model was 25% higher than in the case of the k–ε model.

A transient test case chosen for this study is the one studied experimentally by Lyn [31] at $Re = 21\,400$. The dimensions of the domain are taken to be $20D \times 24D$. Calculations are performed as two dimensional. Three calculation grids are used in order to obtain grid independent solution. Grid sizes are: 6822, 21 800 and 65 397 cells, respectively. Some details of the grids are shown in Figures 13(a)–(c). Grid (b) is an orthogonal grid, and from a numerical point of view represents the simplest grid. The other two grids consist of various cell types and represent 'typical' grids nowadays produced with automatic mesh generators. At the inlet of the solution domain (which is placed at distance of $4.5 \times D$ from the square cylinder), a uniform velocity profile is defined to give the Reynolds number based on cylinder height equal to 21 400. The relative turbulence intensity of 2% (reference is made to the measurements of Lyn [31]) and the ratio of the turbulent to molecular viscosity $(\mu_t/\mu) = 100$ are prescribed and used to calculate turbulence variables at the inlet. At the outlet, a zero gradient condition along the local co-ordinate connecting the interior and boundary cells is employed for all variables. The side and top planes are defined as symmetry planes.

Using fine grids and accurate differencing schemes for the convection term such as AVL SMART (grid (a)) and MINMOD (grids (b) and (c)), it is ensured that numerical error plays a minor role. Following that, the main integral parameters predicted for all three grids

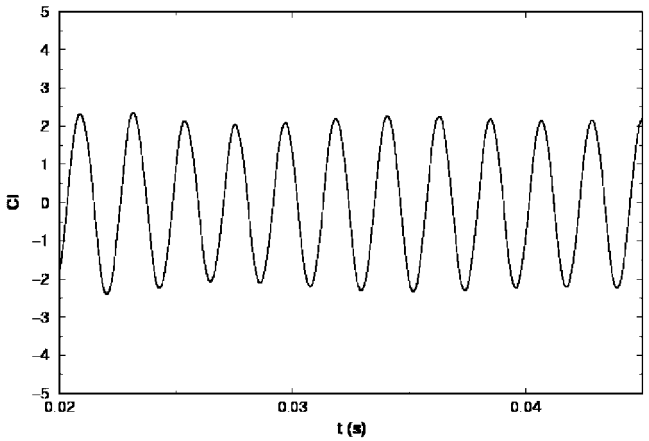

Figure 14. Time evolution of lift coefficient as predicted by RSM.

Table I. Predictions and measurements of integral parameters.

	Cd	Cl′	Str
Present RSM	2.28	1.39	0.141
Franke and Rodi [33], RSM	2.15	—	0.136
Rodi *et al*. [34], LES	2.30	1.15	0.13
Kato and Launder [35], k–ε	2.05	—	0.145
Measurements	2.16–2.28	1.1–1.4	0.130–0.139

do not differ significantly. For example, the full RSM model calculates the time-mean drag coefficients of 2.15, 2.28 and 2.23, respectively. The standard k–ε model also predicts vortex shedding, but it estimates main parameters much lower than measured levels, e.g. $\mathrm{Cd} = 1.8$ and $\mathrm{Str} = 0.119$. Figure 14 shows time histories of lift coefficient for grid (b) as calculated by using RSM model. Table I provides comparisons between present calculations with previous calculations and measurements. A set of measurements [31, 32] is included to provide adequate validation data. The present predictions are close to the measurements, slightly overestimating all integral parameters. The phase averaged data was calculated as suggested by Rodi *et al.* for the Workshop on LES of Flows Past Bluff Bodies [34]. The time period between two successive maximums is divided into 20 equal intervals and the predicted streamlines are compared with the measurements for the same phases (Phase 01, 05, 09 13, 17) as chosen in the Workshop. Nevertheless, Figures 15–19 show a very good agreement between predictions and measurements for each of the phases.

The next example, the Ahmed body [36], is a three-dimensional case where the local grid refinement is employed by using an arbitrary interface, see Figure 20. This idealized vehicle model represents the key benchmark for validation of the turbulence models regarding external

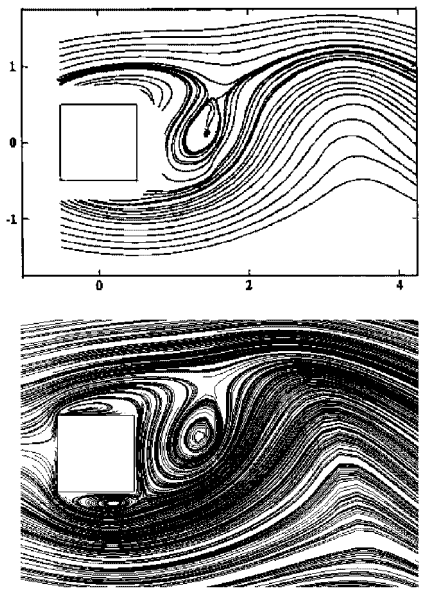

Figure 15. Phase averaged streamlines (Phase 01): measurements (top) and predictions (bottom) with RSM model.

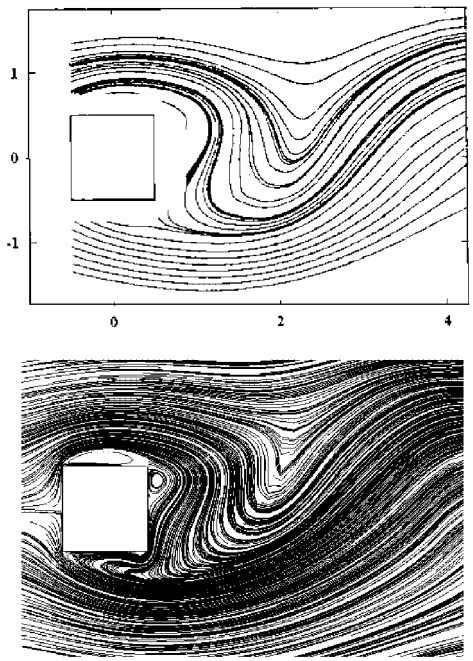

Figure 16. Phase averaged streamlines (Phase 05): measurements (top) and predictions (bottom) with RSM model.

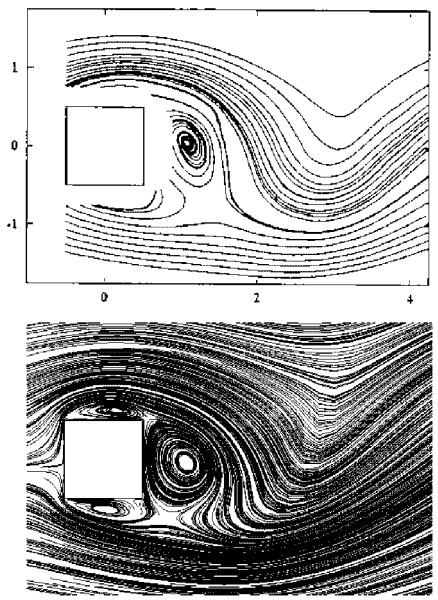

Figure 17. Phase averaged streamlines (Phase 09): measurements (top) and predictions (bottom) with RSM model.

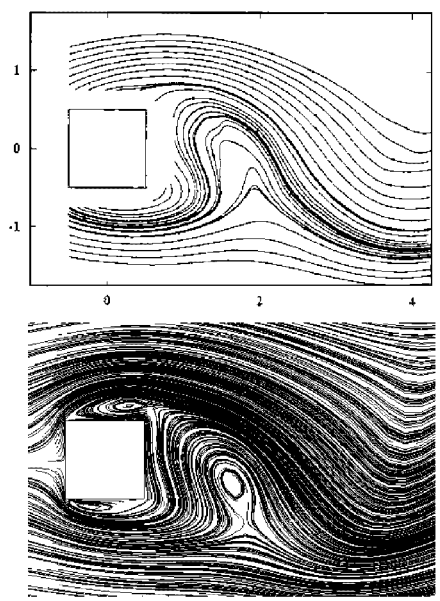

Figure 18. Phase averaged streamlines (Phase 13): measurements (top) and predictions (bottom) with RSM model.

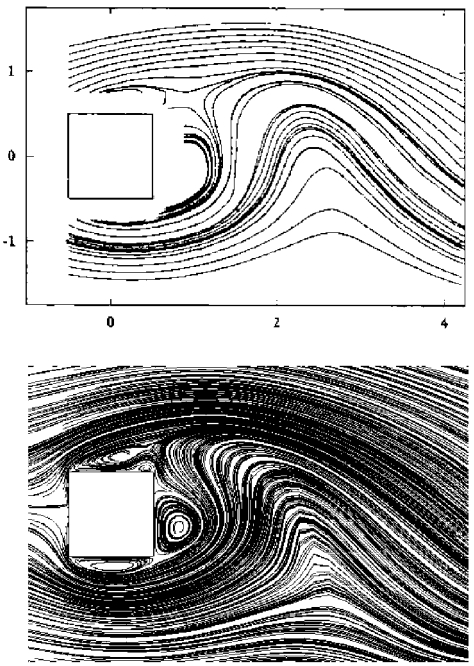

Figure 19. Phase averaged streamlines (Phase 17): measurements (top) and predictions (bottom) with RSM model.

car aerodynamics. This case allows investigation of the back slant effect on the overall drag force. At a certain angle of the slant, a vortex breakdown phenomena appears causing the sudden pressure drop acting on the model. The measurements were recently repeated by Lienhart *et al.* [37] during the course of European project models for vehicle aerodynamics (MOVA). The new data was used in ERCOFTAC Workshop, Jakirlic *et al.* [38], where seven numerical groups provided very different calculation results depending on the calculation grid and the turbulence model used. Therefore, in this work due attention was given to optimize the grid size. The case with the back slant angle of 25° is calculated here. The first step was to find the grid independent solution in two dimension and then to proceed with further meshing by adding the point in the third dimension. The final grid contains 523 000 cells (see Figure 20(a)) mainly hexahedral but also polyhedral cells created along the arbitrary interface. Local grid refinement with the arbitrary interface creates a box around the body ensuring the good grid quality, see Figure 20(b). Despite the work of Basara and Alajbegovic [39] where it is shown that only a transient calculation is appropriate for such a simulation as the vortex shedding is present, here the steady solution is imposed by the employment of the symmetry plane at the mid section of the body, as the aim was only to present a possibility of running RSM on this type of grid. The first next to the wall cells ensure y^+ values on the body to be in the range between 20 and 50. Attention was also given to the inlet boundary conditions. The measured velocity profile was used for extrapolation at the inlet boundary faces. A minimum inlet distance from the Ahmed body has been validated

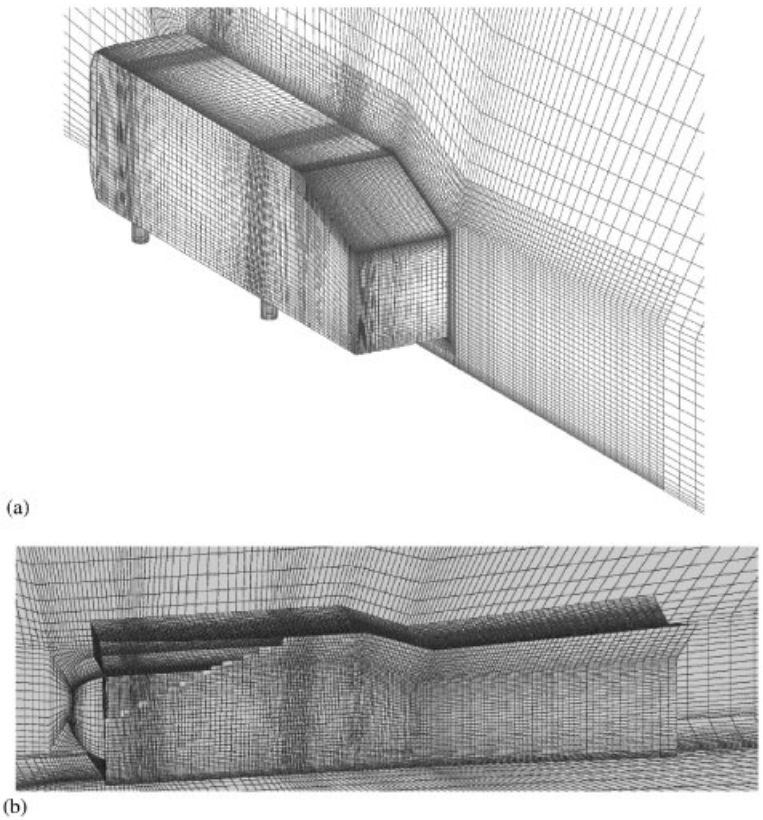

Figure 20. Ahmed body. A computational grid inside (a) and outside (b) of the local refined box.

and it was found that 0.5 m is sufficient in order not to influence results. The best agreement was achieved when the inlet profile was taken from the same set of measurements used for comparisons (inlet profile was taken from $x = -1.443$ m, Lienhart *et al.* [37], the centre of the co-ordinate system is at the end and bottom of the model). The second order MINMOD scheme was used for the present calculations. The chosen profiles for comparisons with the measurements are placed at the symmetry plane on the slant of the body at $x = -0.143$ and -0.063 m, respectively. It is obvious that the k–ε model fails to predict separation on the back slant while the RSM separates but does not attach to the slant again as reported by measurements, see velocity profiles in Figures 21(a) and (b). The normal stress components as shown in Figures 22(a) and (b) are better reproduced by the full Reynolds-stress model though both models produce a larger discrepancy with the measurements. However, looking at iso-lines of the pressure, normal and shear stresses as shown in Figures 23(a)–(c), only small discontinuities can be observed on the arbitrary interface showing that the algorithm proposed here provides appropriate numerical solution.

The next example is a weakly compressible flow in the intake port. The flow structure and the turbulence level in internal engines have a significant effect on the fluid mixing and

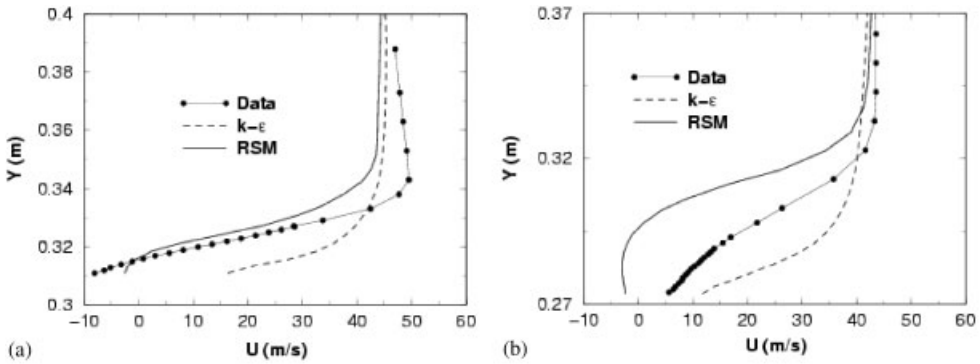

Figure 21. Predicted mean velocity at the location $x = -0.143$ (a) and $x = -0.063$ (b) corresponding to the back slant region of the Ahmed body.

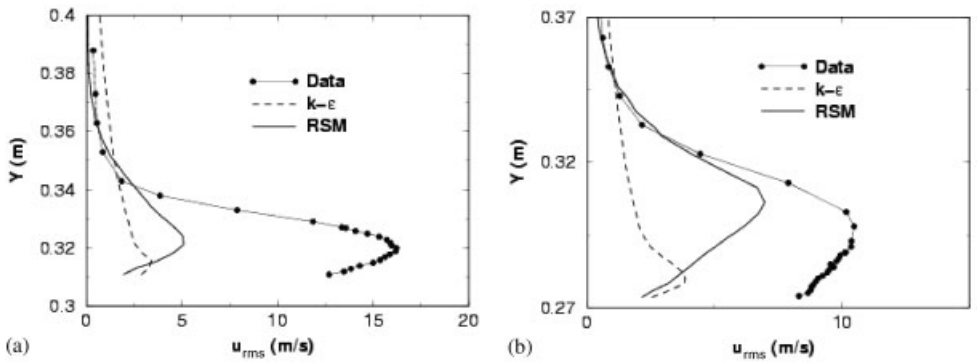

Figure 22. Predicted streamwise turbulence intensity at the location $x = -0.143$ (a) and $x = -0.063$ (b) corresponding to the back slant region of the Ahmed body.

combustion processes. Concerning numerical calculations, it is critical to predict turbulence intensity and it's distribution. Otherwise, the flow field and parameters important for identifying engine's performances can be missed considerably. The most critical position for the turbulence kinetic energy prediction is the region below the valve. Overproduction of turbulence kinetic energy changes the spreading rate of the jet and causes different mixing in the cylinder. Typical intake port configuration and turbulence energy predicted with the RSM model are shown in Figures 24 and 25. The results were obtained on a grid consisting of 222 000 computational cells. The grid employs hexahedral cells distributed near the wall to ensure that $y+$ value is between 30 and 100 in most of the domain. The AVL SMART differencing scheme for convection term [24] was used for the present calculations. The constant static pressure is specified at the outlet and the mass flow is given at the inlet. Calculations are compared with the measurements obtained by LDA at the cylinder cross section in a distance of 1.75D from the bottom of the cylinder head ($D = 0.078$ m). The velocity fields at

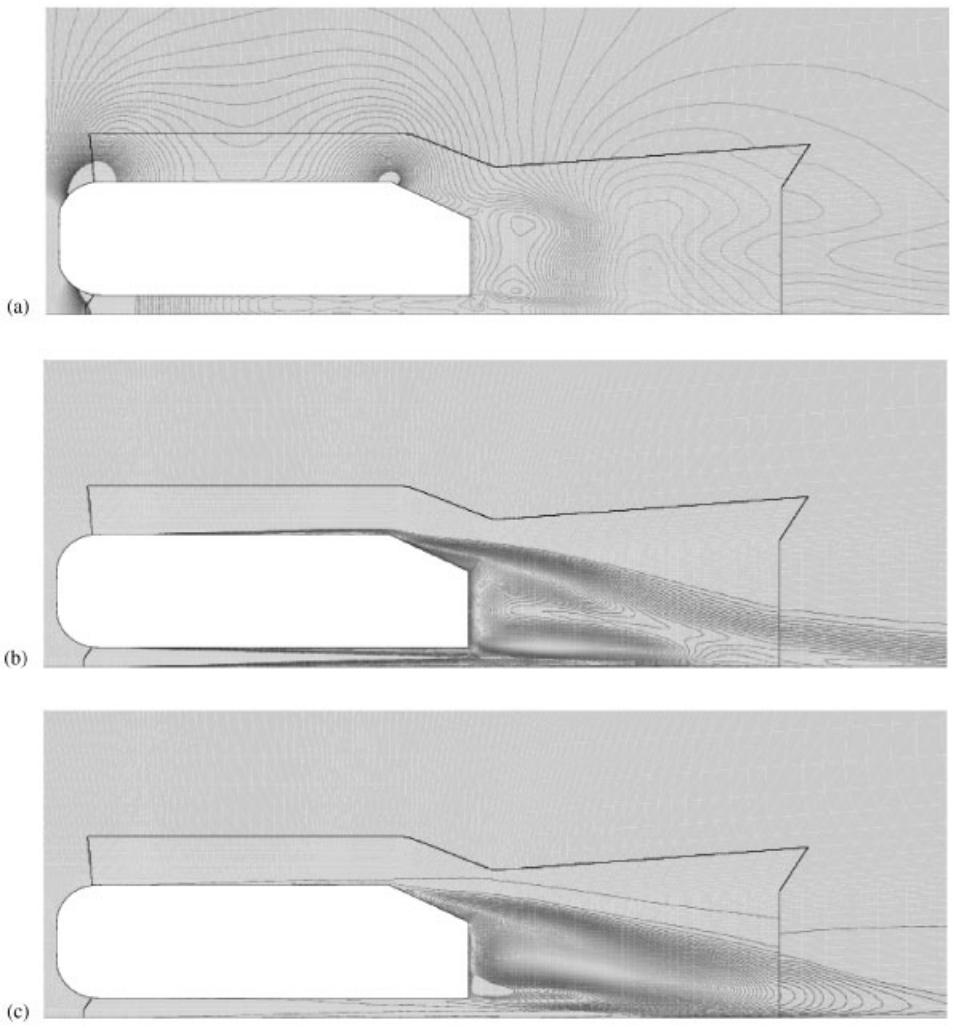

Figure 23. Predicted iso-lines of the pressure (a), $\overline{u^2}$ normal (b) and shear $\overline{uv}$ stress components.

the measured cross section as predicted by k–ε and RSM are shown in Plate 1(a–c). Velocity vectors are shown at certain radial positions which do not represent the positions of computational cells, only to allow easier comparisons with the measurements. A stronger swirl motion predicted by the k–ε model can be observed. This is also confirmed by the global parameters summarized in Table II. The RSM model predicts all parameters better than the k–ε model but there is still visible disagreement with the measurements. The blame can probably be placed on the standard wall function used in conjunction with the both of the models. The calculations with the full Reynolds-stress model were almost three times slower than with the k–ε model.

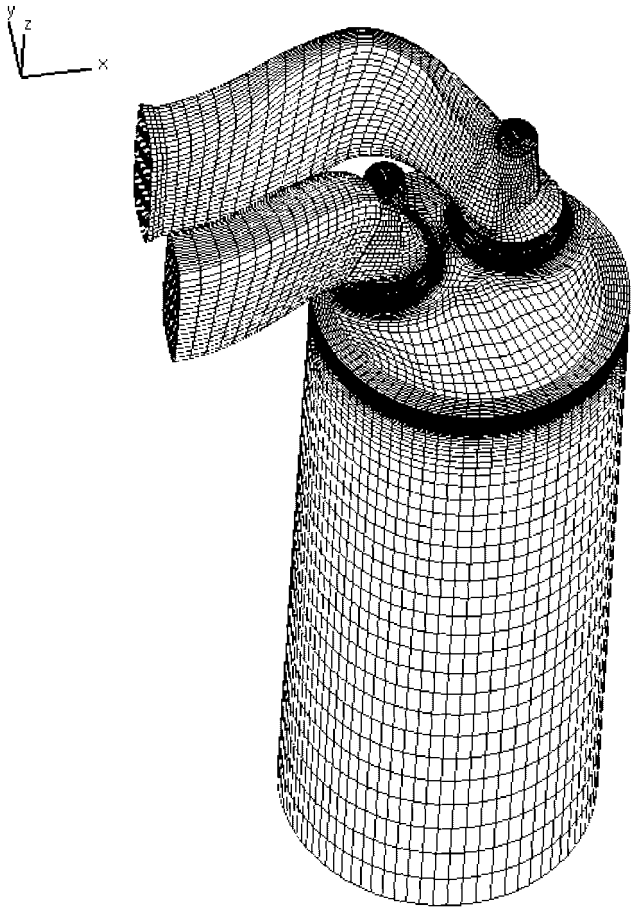

Figure 24. Intake port. Computational domain and grid.

5. CONCLUSIONS

The method for the implementation of the second-moment closure into a polyhedral finite volume approach is reported in this paper. In comparison to previous publications, the main issues are done differently: a discretization of diffusion terms in all equations (especially important for momentum equations), a coupling procedure for the velocity and pressure where stresses are not included but rather $\frac{2}{3}k$ and the new wall approach for the Reynolds-stresses. The variety of different flows were predicted by the second-moment closure: a fully developed boundary layer in a plane and curved channel, steady and transient separating flows, two and three-dimensional flows, incompressible and weakly compressible flows. Different grids were used for the calculations: hexahedral body fitted grids, hybrid grids including all types of cells up to six faces and the grids with polyhedral cells created at the arbitrary interface. Therefore, it was shown that the second-moment closure can be efficiently applied on any

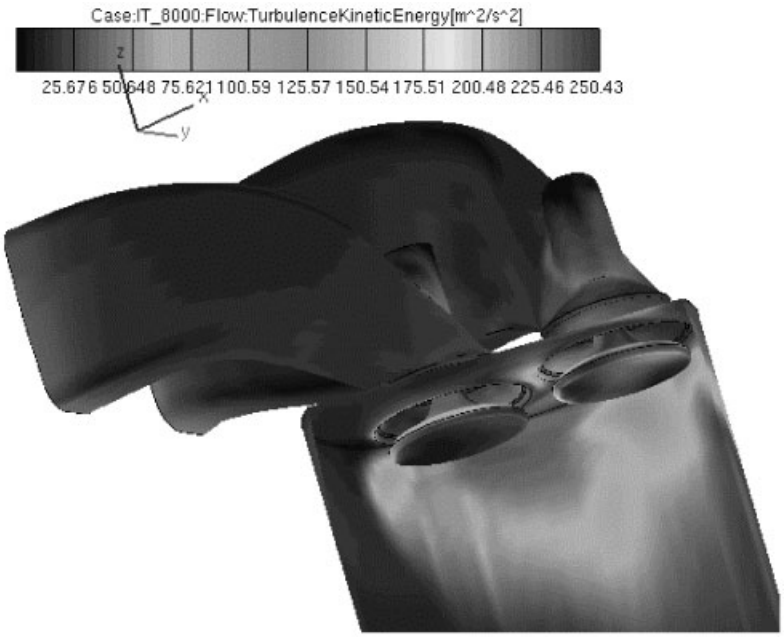

Figure 25. Predicted turbulence kinetic energy by the RSM.

Table II. Measured and calculated engine parameters (Mt—torque, SN—swirl number, μ_σ—discharge coefficient).

	μ_σ	Mt	SN
Data	0.473	0.12	1.646
k–ε	0.45	0.0158	2.01
RSM	0.4625	0.142	1.80

arbitrary unstructured grid. The numerical algorithm proposed in this paper is simple, easy to incorporate in existing Navier–Stokes type of codes and obviously robust enough to be also used for industrial applications.

REFERENCES

1. Obi S, Peric M, Scheuerer G. A finite volume calculation procedure for turbulent flows with second-order closure and coloacated variable arrangement. *Proceedings of the 7th Symposium on Turbulent Shear Flows*, Stanford University, USA, 1989.
2. Lien FS, Leschziner MA. Second-moment modelling of recirculating, flows with a non-orthogonal collocated finite-volume algorithm. In *Turbulent Shear Flows*, Durst *et al.* (eds). 1993; **8**:205–222.
3. Farnanieh B, Davidson L, Sunden B. Employment of second-moment closure for calculation of turbulent recirculating flows in complex geometries with collocated variable arrangement. *International Journal for Numerical Methods in Fluids* 1993; **16**:525.
4. Lai YG. Computational method of second-moment closure in complex geometries. *AIAA Journal* 1995; **33**:1426.

5. Rhie CM, Chow WL. Numerical study of the turbulent flow past an airfoil with trailing edge separation. *AIAA Journal* 1983; **21**:1525–1532.
6. Demirdzic I, Muzaferija S. Numerical method for coupled fluid flow, heat transfer and stress analysis using unstructured moving meshes with cells of arbitrary topology. *Computer Methods in Applied Mechanics and Engineering* 1995; **125**:235–255.
7. Ferziger JH, Peric M. *Computational Methods for Fluid Dynamics*. Springer: Berlin, 1996.
8. Marthur SR, Murthy JY. A pressure based method for unstructured meshes. *Numerical Heat Transfer B*, 1997; **31**:195–215.
9. Speziale CG, Sarkar S, Gatski TB. Modeling the pressure-strain correlation of turbulence, an invariant dynamical systems approach. *Journal of Fluid Mechanics* 1991; **227**:45–272.
10. Launder BE, Spalding DB. The numerical computation of turbulent flows. *Computer Methods in Applied Mechanics and Engineering* 1974: **3**:269–289.
11. Muzaferija S. Adaptive finite volume method for flow predictions using unstructured meshes and multigrid approach. *Ph.D. Thesis*, Imperial College, University of London, UK, 1994.
12. Basara B. A numerical study into the effects of turbulent flows around full-scale buildings. *Ph.D. Thesis*, City University of London, UK, 1993.
13. Basara B. Two-layer model combining the Reynolds-stress model with the low Re-number k–ε model near the wall. *ASME paper*, *1998-4896*, 1998.
14. Peric M. A finite volume method for the prediction of three-dimensional fluid flows in complex ducts. *Ph.D. Thesis*, University of London, UK, 1985.
15. Patankar SV, Spalding DB. A calculation procedure for heat, mass and momentum transfer in three-dimensional parabolic flows. *International Journal of Heat Mass Transfer* 1972; **15**:1510–1520.
16. Obi S. Berechnung komplexer turbulenter Strömungen mit einem Reynolds-Spannungs-Modell. w predictions using unstructured meshes and multigrid approach. *Ph.D. Thesis*, University of Erlangen, Germany, 1991.
17. Lien FS, Leschziner MA. A general non-orthogonal collocated finite volume algorithm for turbulent flow at all speeds incorporating second-moment turbulence-transport closure, Part 1: Computational implementation. *Computer Methods in Applied Mechanics and Engineering* 1994; **114**:123–148.
18. Basara B, Younis BA. Assessment of the SSG pressure-strain model in two-dimensional turbulent separated flows. *Applied Scientific Research* 1995; **55**:39–61.
19. Hanjalic K, Jakirlic S. Contribution towards the second-moment closure modelling of separating turbulent flows. *Computers and Fluids* 1998; **22**(2):137–156.
20. Lasher WC, Taulbee DB. On the computation of turbulent back-step flow. *International Journal of Heat and Fluid Flow* 1992; **1**:30–40.
21. Basara B. Computations of automotive flows using the second-moment closure. *Proceedings of ECCOMAS 2000*, Barcelona, Spain, September 11–14, 2000.
22. Kim J, Moin P, Moser R. Turbulence statistics in fully developed channel flow at the low Reynolds number. *Journal of Fluid Mechanics* 1987; **177**:133–166.
23. Hunt IA, Joubert PN. Effects of small streamline curvature on turbulent duct flow. *Journal of Fluid Mechanics* 1979; **91**:633–658.
24. Przulj V, Basara B. Bounded convection schemes for unstructured grids. *AIAA Paper 2001-2593*, 2001.
25. Sweby PK. High resolution schemes using flux limiters for hyperbolic conservation laws. *SIAM Journal on Numerical Analysis* 1984; **21**:995–1011.
26. Van der Vorst. Bi-CGSTAB: A fast and smoothly converging variant of Bi-CG for the solution of nonsymmetric linear system. *SIAM Journal on Scientific Computing* 1992; **13**:631–644.
27. Meijerink JA, Van der Vorst HA. Guidelines for the usage of incomplete decompositions in solving sets of linear equations as they occur in practical problems. *Journal of Computational Physics* 1981; **44**:134–155.
28. Monson DJ, Seegmiller HL, McConnaughey PK. Comparison of LDV measurements and Navier–Stokes equations in a two-dimensional 180-degree turn-around duct. *AIAA Paper 89-0275*, Reno, Nevada, 1989.
29. Basara B, Cokljat D, Younis BA. Assessment of eddy-viscosity and Reynolds-stress transport closures in two- and three-dimensional turn-around ducts. *ASME FED* 1995; **217**:249–256.
30. Shur ML, Strelets MK, Travin AK, Spalart PR. Turbulence modelling in rotating and curved channels: assessing the Spalart-Shur correction. *AIAA Journal* 2000; **38**(5):784–792.
31. Lyn DA. Ensemble-averaged measurements in the turbulent near wake of a square cylinder: a Guide to the data. *Report CE-HSE-92*-6, School of Civil Engineering, Purdue University, USA, 1992.
32. Bearmen PW, Obasaju ED. An experimental study of pressure fluctuations on fixed and oscillating square cylinders. *Journal of Fluid Mechanics* 1982; **119**:297.
33. Franke R, Rodi W. Calculation of vortex shedding past a square cylinder. *Proceedings of 8th Symposium on Turbulent Shear Flows*, Munich, Germany, 1991.
34. Rodi W, Ferziger JH, Breuer M, Pourquie M. Status of large Eddy simulation: results of a workshop. *Journal of Fluids Engineering* 1997; **119**:248.
35. Kato M, Launder BE. The modeling of turbulent flow around stationary and vibrating square cylinder. *Proceedings of 9th Symposium on Turbulent Shear Flows*, Kyoto, Japan, 1993.

36. Ahmed SR, Ramm G, Faltin G. Some salient features of the time-averaged ground vehicle wake. *SAE paper 840300*, Detroit, USA, 1984.
37. Lienhart H, Stoots C, Becker S. Flow and turbulence structures in the wake of a simplified car model (Ahmed Model). *Notes on Numerical Fluid Mechanics*, Wagner *et al.* (eds). 2002; **77**:323–330.
38. Jakirlic S, Jester-Zurker R, Tropea C. *Proceedings of the 9th ERCOFTAC/IAHR/COST Workshop on Refined Turbulence Modelling*, Darmstadt, Germany, 2001.
39. Basara B, Alajbegovic A. Steady state calculations of turbulent flows around Morel Body. *Proceedings of the 7th International Symposium on Flow Modelling and Fluid Measurements*, Tainan, Taiwan, October 5–8, 1998.

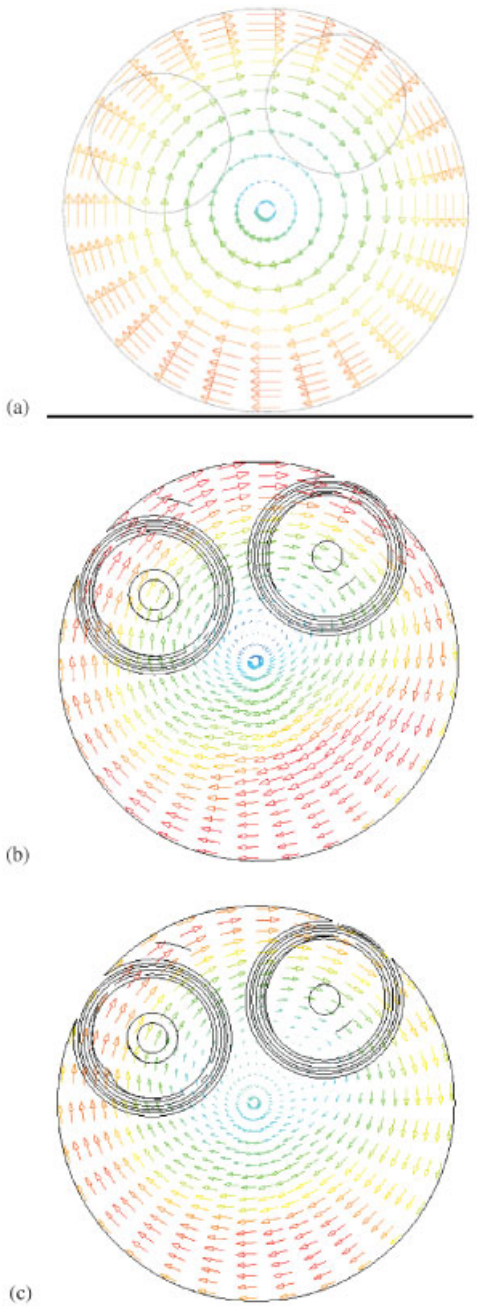

Plate 1. Velocity vectors projected at the cross section as provided by measurements (a), and predicted by k–ε (b) and RSM (c) models.